Supporting Information

Rheology and Dynamics of Solvent Segregation Driven Gel (SeedGel)

Yuyin Xi [1,2], Ryan P. Murphy [1], Qingteng Zhang [3], Aurora Zemborain [4], Suresh Narayanan [3], Junsu Chae [5], Siyoung Q. Choi [5], Andrei Fluerasu [6], Lutz Wiegart [6], Yun Liu [1,2,7*]

Email: yunliu@udel.edu or yun.liu@nist.gov

1. Center for Neutron Research, National Institute of Standards and Technology, Gaithersburg, MD, 20899, USA
2. Department of Chemical & Biomolecular Engineering, University of Delaware, Newark, DE, 19716, USA
3. X-ray Science Division, Argonne National Laboratory, Argonne, IL 60439, USA
4. Pritzker School of Molecular Engineering, University of Chicago, Chicago, IL 60637, USA
5. Department of Chemical and Biomolecular Engineering, Korea Advanced Institute of Science and Technology (KAIST), Daejeon 34141, Republic of Korea
6. National Synchrotron Light Source II, Brookhaven National Laboratory, Upton, New York 11973, United States
7. Department of Physics & Astronomy, University of Delaware, Newark, DE, 19716, USA

1. Determination of linear viscoelastic region of SeedGel

Figure S1 below shows the amplitude sweep of SeedGel at different temperatures. The results suggest that the 0.1 % shear strain used in the small amplitude oscillatory shear (SAOS) measurements is within the linear viscoelastic region of SeedGel.
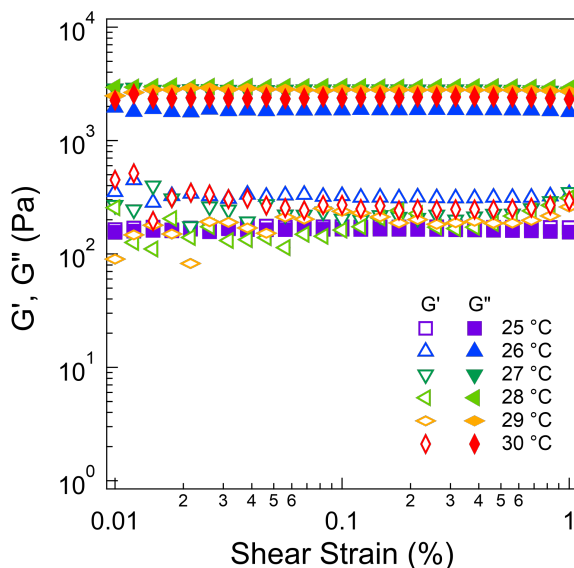
Figure S1. The storage and loss moduli of SeedGel as a function of shear strain at different temperatures. The angular frequency is fixed at 1 rad/s. The error bars are estimated from the torque limit of the rheometer and are often smaller than the symbol size.

2. Structures of SeedGel probed by small-angle X-ray scattering (SAXS)

Figure S2 shows the SAXS patterns of SeedGel collected in the temperature range between 28 ˚C and 36 ˚C. The scattering profiles are almost identical to each other at different temperatures. As X-rays are mainly sensitive to scattering from the silica nanoparticles in our samples, this indicates that the structures of the particle domain and the local packing of particles remain almost the same in this temperature range.
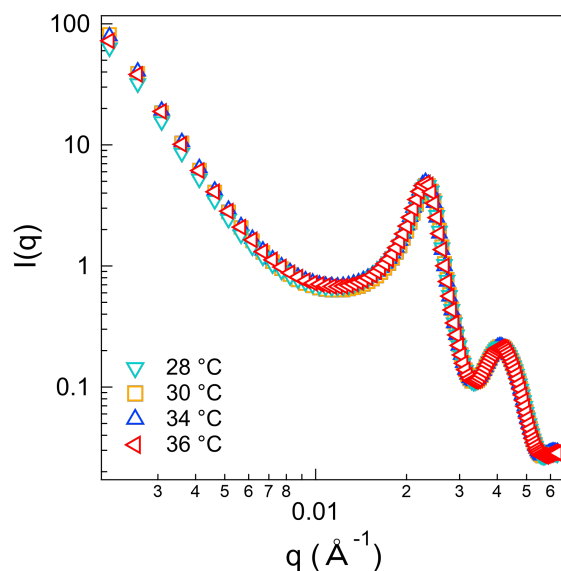

Figure S2. Small angle X-ray scattering intensity of SeedGel plotted against wavevector, q. The SAXS profiles are almost identical in the temperature range between 28 ˚C and 36 ˚C.

3. Validation of the interpretation of the intensity change at $q = 0.04$ Å^{-1}

When analyzing the SANS patterns, the form factor is approximated with a sphere model while the structure factor is calculated using the Hayter-Penfold method.[1–5] The fitting is performed in SASview and β-approximation is used to account for the size polydispersity of the particles. [4,6] The scattering length density of the solvent, the volume fraction of particles in the particle domain (structure factor volume fraction), and the number of charges on the particle surface are left as variables, and the rest of the parameters are fixed during the fitting. The scale factor is determined by the ratio of the total particle volume fraction (form factor volume fraction) over

the structure volume fraction of the particles and is not a fitting parameter. (SasView includes the structure factor volume fraction as a scaling factor when including the structure factor in the data analysis. Therefore, the definition of the scaling factor is slightly different from cases when only using the form factor to analyze the data with the SasView.) The nominal volume fraction in a sample is calibrated using the scattering data of the Ludox TM stock solution and silica nanoparticle volume fraction in Ludox TM determined by the mass density measurement. According to the factorization theory, the scattering intensity can be modeled with number density (n), form factor (P(q)), and structure factor (S(q)) as shown in Eq-S1. For spherical scatters, the intensity can be rewritten as in Eq-S2. Here, φ is the volume fraction of nanoparticles in the sample (form factor volume fraction), v is the volume of an individual particle, $\Delta\rho$ is the scattering length density difference between the particle and the surrounding solvent, and r is the radius of the particle, and *background* is the background level. Figure S3 shows the fitting results of the SeedGel sample at 26 ˚C, 30 ˚C, and 34 ˚C. The results show that the model fits the scattering data well and the intensity difference between different temperatures at around q = 0.04 Å^{-1} is captured by the model.

$$I(q) = nP(q)S(q) + background \qquad \text{Eq-S1}$$

$$I(q) = \varphi v(\Delta\rho)^2 \left[\frac{3(\sin(qr) - qr\cos(qr))}{(qr)^3}\right]^2 S(q) + background \qquad \text{Eq-S2}$$

The structure factors at different temperatures are plotted in Figure S4 (a). The structure factor curves crossover at around q = 0.04 Å^{-1}, which is the q-position we used to compare the intensity change at different temperatures in the main text. There is almost no change in the structure factor at q = 0.04 Å^{-1}, which is clearly shown in the zoomed-in image in the inset picture. The change of the scattering intensity is thus due to the contrast change of the sample at different temperatures at q = 0.04 Å^{-1}. This confirms the validity of the way we use to interpret our scattering data in the paper.

We further plotted the normalized SANS scattering intensity as a function of temperature over a wide q-range between 0.03656 Å^{-1} and 0.05779 Å^{-1}, which covers the scattering peak at q = 0.04 Å^{-1} (Figure S4 (b)). The intensity at higher temperatures is normalized to that at 20 ˚C. The normalized intensity thus corresponds to the contrast multiplied by the normalized structure factor. From Figure S4 (a), the structure factor increases with the increase of the temperature at q-positions larger than q = 0.04 Å^{-1}, whereas it decreases at elevated temperatures at q-positions smaller than q = 0.04 Å^{-1}. The normalized intensities (Figure S4 (b)) show the same transition temperature at all the q-positions, both smaller and larger than q = 0.04 Å^{-1}, indicating that the change of contrast plays a dominant role in determining the scattering intensity. Also, after gelation (above 26 °C), the normalized intensity keeps increasing (Figure S4 (b)), whereas the structure factor maintains the same values (Figure S4 (a)). It also supports our conclusion that the change of intensity at q = 0.04 Å^{-1} results from the contrast change.

Moreover, the scattering length density (SLD) of the solvent surrounding the particle extracted from the fitting is plotted in Figure S5 (a) as a function of temperature. The change of SLD shows the same trend as that shown in Figure 2 in the main text, which confirms again that the intensity change at q = 0.04 Å^{-1} is mainly due to the contrast change between the particle and the

surrounding solvent. The volume fraction of the water content in the particle domain can also be estimated using the solvent SLD (Figure S5 (b)). It is important to note that the SLD obtained from the fits is biased by the model, which may introduce systematic errors in the absolute values of the inferred water content in the particle domain. However, the trend of the SLD change as a function of temperature is not affected by this.

The particle concentration within the particle domain can also be obtained through the fitting and is plotted as a function of the temperature in Figure S6. The concentration of particles maintains almost constant at about 46 % in the gel state. Again, the exact value of the particle concentration may be biased by the model we chose to fit the results, but the trend as a function of temperature is reliable. In contrast, the particle concentration in the solvent domain is expected to be very small, if there is any, based on some previous studies.[7–10] For a similar system but with much smaller particle concentrations, it is found that silica particles can aggregate quickly and precipitate out of solutions. When the sample temperature is about a couple of degrees above the aggregation temperature, there is almost no dispersed particles in the solvent. [9,10] Based on our SANS experiment in this paper, the aggregation temperature is around 24 ºC and the gelation temperature is about 26 ºC. Hence, it is reasonable to believe that most particles should be part of the particle domain in the gel state. Also, the data analysis of SANS pattern in previous publications together with the analysis approach used here show that the particle volume fractions of the particle domain is consistent with the fact that almost all particles are in the particle domain. [11] In addition, by assuming that there are no particles in the solvent domain, the calculated refractive index of the particle and solvent doamins explains well the observed optical properties of a SeedGel in a previous study. [8] Therefore, all these experimental results are consistent with the fact that the particle concentration in the solvent domain is extremely low, if there is any.

With the SLD of the solvent in the particle domain obtained from the fitting, the composition of the species in each domain could be determined based on mass balance. The averaged SLD of each domain and their contrast ($\Delta\rho$) could be calculated as well. By fitting the low-q region of the SANS data, the specific surface area of the SeedGel sample could be determined using Eq-S3. [12,13] Here, S is the surface area and V is the sample volume. It is found that the specific surface area of the SeedGel sample barely changes and stays within the range of 0.25 m^2/g and 0.3 m^2/g.

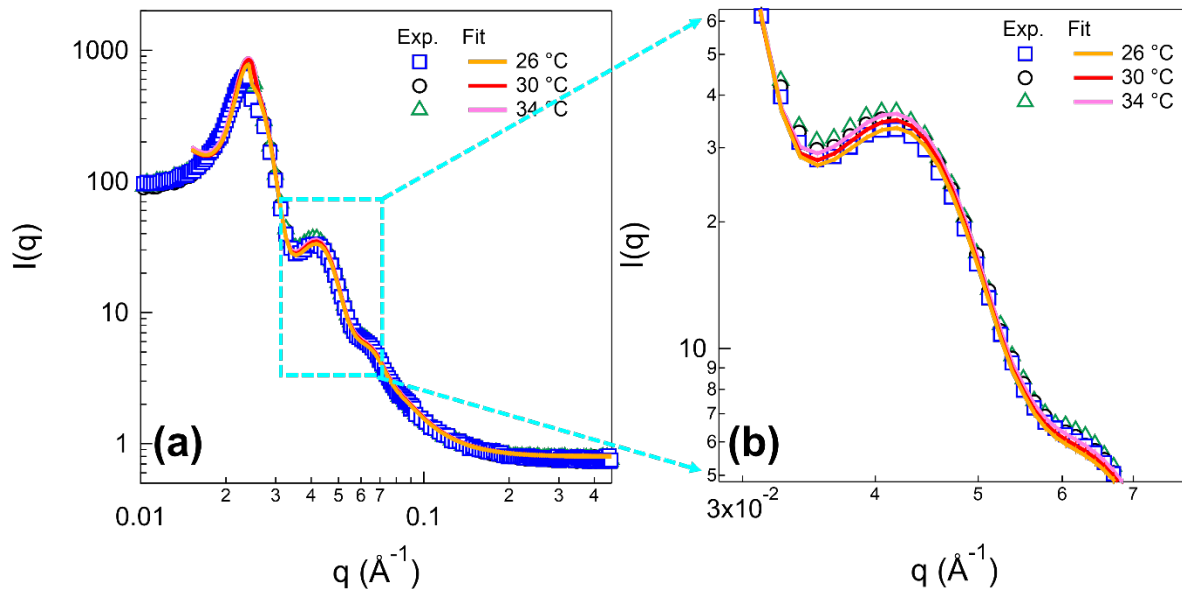$$I\ (q) = \frac{2\pi(\Delta\rho)^2}{q^4}\frac{S}{V} + Background \qquad\qquad \text{Eq-S3}$$

Figure S3 (a) SANS data and the corresponding fittings using sphere model with Hayter-Penfold method at 26 °C, 30 °C, and 34 °C. (b) the zoomed-in plot of the region in the dashed box in (a).
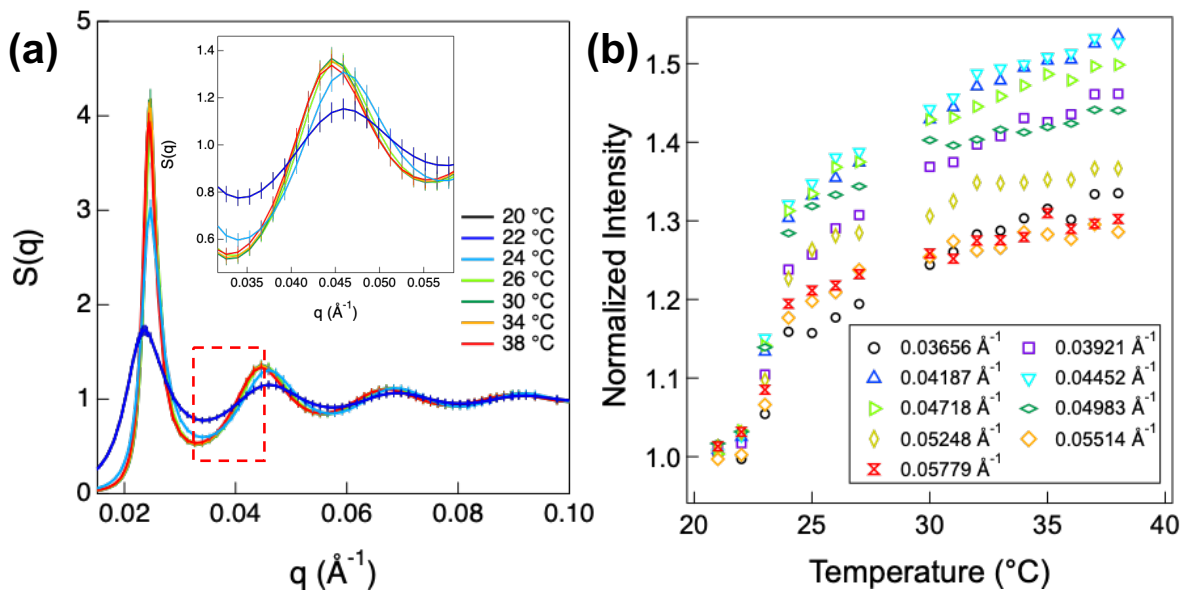

Figure S4 (a) Structure factor extrapolated from the fitting of the SANS results at temperatures between 20 °C and 38 °C. The inset image shows the zoomed-in region of the red dashed box. (b) The intensities normalized to that 20 °C at different temperatures over the q-range of 0.03656 Å⁻¹ and 0.05779 Å⁻¹.
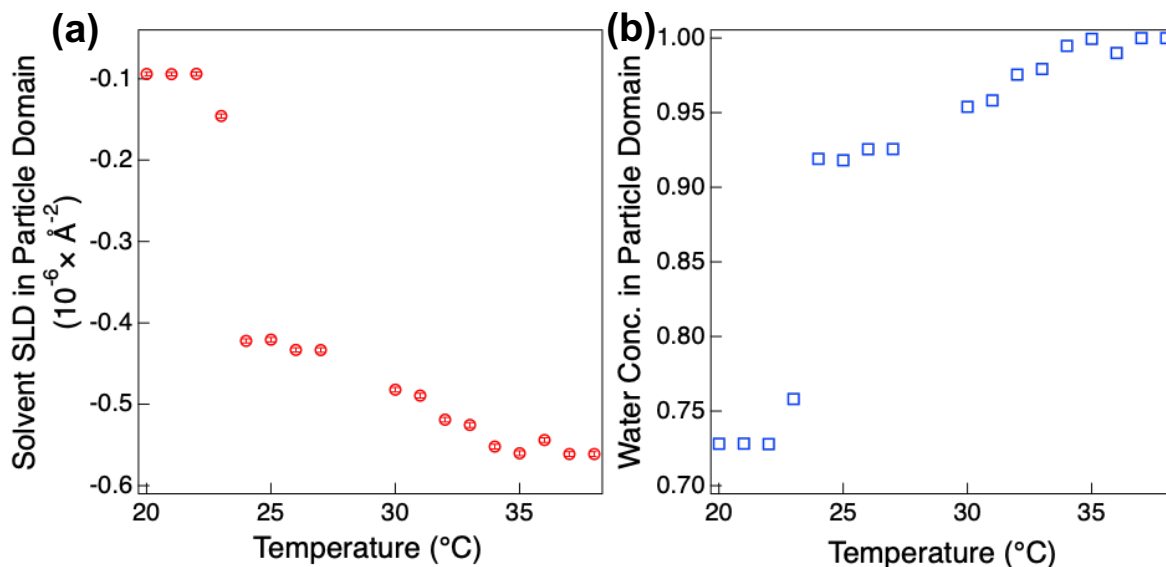
Figure S5 (a) The fitted scattering length density of the solvent in the particle domain as a function of temperature. (b) The corresponding water concentration in the particle domain.
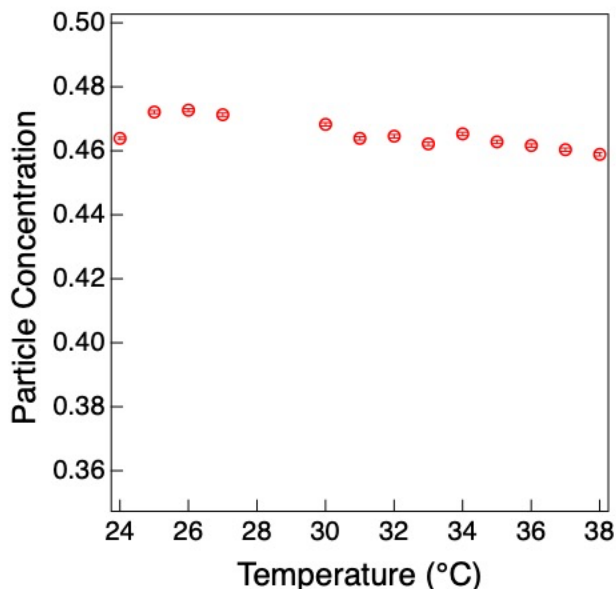

Figure S6 Particle concentration in the particle domain as a function of temperature obtained from the SANS fitting using the Hayter-Penfold structure factor.

4. Reproducibility of the autocorrelation function (g_2) at different temperatures

During the XPCS experiments, five different measurements are performed at different spots of the same sample for each temperature. The results are shown in Figure S7. The third measurement at 26 ˚C and 34 ˚C, and the fourth measurement at 30 ˚C are selected to plot in Figure 4 in the main text. Their fitting results are shown in Figure 5 and Figure 6 in the main text. The fitting results of all the measurement results are shown here from Figure S10 to Figure S13.
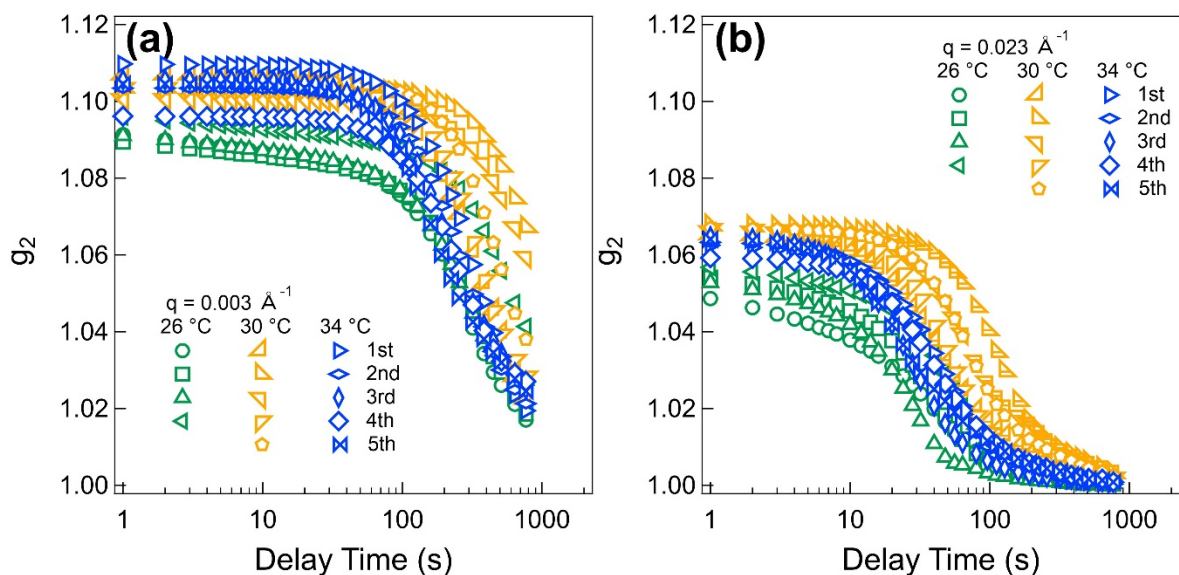
Figure S7. The autocorrelation functions of SeedGel at five different locations at (a) $q = 0.003$ Å^{-1} and (b) $q = 0.023$ Å^{-1}. Three temperatures are measured, and the error bars are often smaller than the symbol size.

5. Stability of SAXS during the XPCS measurements

The stability plots in Figure S8 indicate that the scattering intensity does not change during the XPCS measurements.
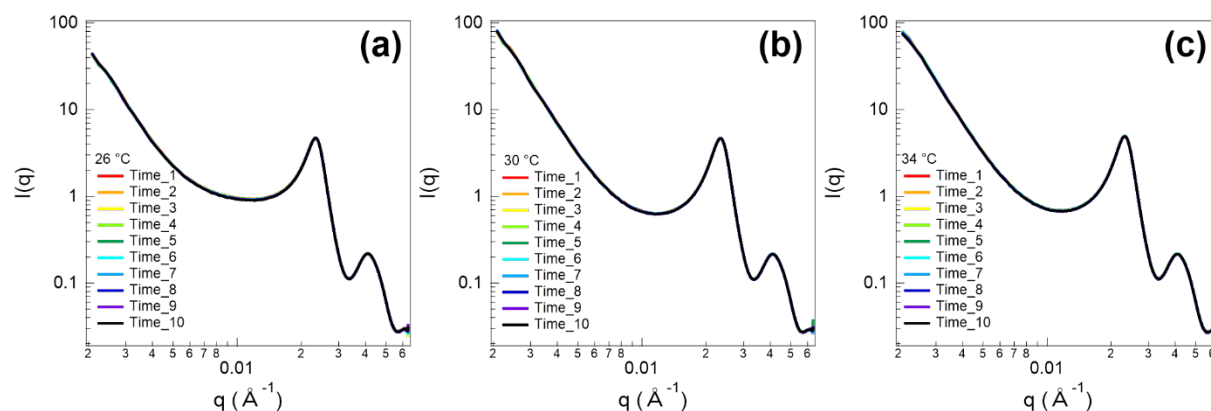

Figure S8. Stability of the SAXS intensity for each autocorrelation measurement at (a) 26 ˚C, (b) 30 ˚C, and (c) 34 ˚C. For each of the autocorrelation measurements, the frames are divided into 10 slices based on time. The integration of the intensities of all frames within one slide results in one scattering profile in the above figures.

6. Calculation of Bkg (q) based on 1-D SAXS data

For an ideal XPCS instrument when the q resolution is very narrow, Bkg $(q)=1$. In reality, the scattering data obtained from an experiment need to be grouped into a set of discrete q's with a finite resolution to improve the data statistics. The deviation of Bkg (q) from 1 originates from

the finite size of each q-value. The smaller the q resolution, the less the deviation is. We proposed the following method to estimate the $g_2(q)$ background value using the experimentally obtained SAXS data.

To demonstrate the calculation of the deviation of $Bkg\ (q)$ from 1, the 1-D scattering profile from SeedGel at 30 °C was used. Within the q-range that the detector probes, 360 q-values are used (i.e. q_n). Within each q window, all the pixels are integrated and averaged to obtain the intensity $I(q_n)$. [14] Eq-S4 below derives g_2 from the original equation and it can be approximated using the intensity at each q-position. Here, as we are calculating the deviation of $Bkg\ (q)$ from 1, the $I(t)$ and $I(t + \Delta t)$ are uncorrelated. The intensity recorded from scattering data $I(q_n)$ can be used to represent the time averaged intensity $\langle I(t)\rangle_t$ (i.e. ($\langle I(t)\rangle_t = \langle I(t + \Delta t)\rangle_t = I(q_n)$).

$$Bkg\ (q) = \frac{\langle\langle I(t)I(t + \Delta t)\rangle_t\rangle_p}{\langle\langle I(t)\rangle_t\rangle_p\langle\langle I(\ t + \Delta t)\rangle_t\rangle_p}$$

$$= \frac{\langle\langle I(t)\rangle_t\langle I(t + \Delta t)\rangle_t\rangle_p}{\langle\langle I(t)\rangle_t\rangle_p\langle\langle I(\ t + \Delta t)\rangle_t\rangle_p}$$

$$= \frac{\langle I(q_n)^2\rangle_p}{(\langle I(q_n)\rangle_p)^2}$$

$$= 1 + \frac{\langle I(q_n)^2\rangle_p - (\langle I(q_n)\rangle_p)^2}{(\langle I(q_n)\rangle_p)^2}$$

$$= 1 + \frac{\langle((I(q_n) - \langle I(q_n)\rangle_p)^2\rangle_p}{(\langle I(q_n)\rangle_p)^2} \qquad \text{Eq-S4}$$

In Eq-S4, $\langle I(q_n)\rangle_p$ is the averaged intensity over all pixels for a finite q value used in the data reduction, and is simply the experimentally measured intensity at each q-position. In order to calculate the term $\langle((I(q_n) - \langle I(q_n)\rangle_p)^2\rangle_p$, the intensity in the vicinity of q_n needs to be acquired. For a random scattering profile, it is assumed that slopes of the scattering profile between q_n and q_{n+1} are constant values s_n, shown in Eq-S5. The region between $\frac{q_n + q_{n-1}}{2}$ and $\frac{q_{n+1} + q_n}{2}$ are used to extrapolate the intensities near q_n. Eq-S6 and Eq-S7 describe the detailed steps to derive the relation between $g_2(q)$ and $I(q_n)$.

$$s_n = \frac{I(q_{n+1}) - I(q_n)}{q_{n+1} - q_n} \qquad \text{Eq-S5}$$

$$\langle\left((I(q_n) - \langle I(q_n)\rangle_p\right)^2\rangle_p = \frac{\int_{\frac{q_n + q_{n-1}}{2}}^{q_n} s_{n-1}^2(q - q_n)^2 dq + \int_{q_n}^{\frac{q_{n+1} + q_n}{2}} s_n^2(q - q_n)^2 dq}{\frac{q_{n+1} + q_n}{2} - \frac{q_n + q_{n-1}}{2}}$$

$$= \frac{-\frac{1}{3}s_{n-1}^2\left(\frac{q_n + q_{n-1}}{2} - q_n\right)^3 + \frac{1}{3}s_n^2\left(\frac{q_{n+1} + q_n}{2} - q_n\right)^3}{\frac{q_{n+1} - q_{n-1}}{2}}$$

$$= \frac{\frac{1}{24}s_{n-1}^2(q_n - q_{n-1})^3 + \frac{1}{24}s_n^2(q_{n+1} - q_n)^3}{\frac{q_{n+1} - q_{n-1}}{2}}$$

$$= \frac{\left(\frac{I(q_n)-I(q_{n-1})}{q_n-q_{n-1}}\right)^2 (q_n-q_{n-1})^3 + \left(\frac{I(q_{n+1})-I(q_n)}{q_{n+1}-q_n}\right)^2 (q_{n+1}-q_n)^3}{12(q_{n+1}-q_{n-1})}$$

$$= \frac{(I(q_n)-I(q_{n-1}))^2(q_n-q_{n-1}) + (I(q_{n+1})-I(q_n))^2(q_{n+1}-q_n)}{12(q_{n+1}-q_{n-1})} \qquad \text{Eq-S6}$$

$$\therefore\ g_2\big(q,\Delta t = \infty\big) = 1 + \frac{\langle((I(q_n)-\langle I(q_n)\rangle_p)^2\rangle_p}{(\langle I(q_n)\rangle_p)^2} = 1 +$$

$$\frac{(I(q_n)-I(q_{n-1}))^2(q_n-q_{n-1}) + (I(q_{n+1})-I(q_n))^2(q_{n+1}-q_n)}{12I(q_n)^2(q_{n+1}-q_{n-1})} \qquad \text{Eq-S7}$$

7. Calculation of $g_2\big(q, \infty\big)$ using an analytical formula I(q)=q⁻⁴

To test the accuracy of the approximation with constant slopes between neighboring points, we used an analytical expression that I(q) = q⁻⁴. As discussed in our previous publications, the q⁻⁴ decay at the low-q range is known in SeedGel. [7,11] The detailed derivations are shown in Eq-S8 and Eq-S9. It is found that the deviation of $Bkg\ (q)$ calculated from SAXS data and analytical expression are very close to each other (Figure S5). The largest deviation occurs at the lowest q values for SeedGel, which is about 0.007. As every 10 of the g_2 from 360 q-values will be averaged to result in a better signal-to-noise ratio, the g_2 background in our fitting is allowed to deviate 0.005 from 1.

$$\langle\big((I(q_n) - \langle I(q_n)\rangle_p\big)^2\rangle_p = \langle\left(\frac{1}{q^4} - \frac{1}{q_n^4}\right)^2 \rangle_p$$

$$= \frac{\int_{\frac{q_n+q_{n-1}}{2}}^{\frac{q_{n+1}+q_n}{2}} \left(\frac{1}{q^4} - \frac{1}{q_n^4}\right)^2 dq}{\frac{q_{n+1}+q_n}{2} - \frac{q_n+q_{n-1}}{2}}$$

$$= \frac{\int_{\frac{q_n+q_{n-1}}{2}}^{\frac{q_{n+1}+q_n}{2}} (q^{-8} - 2q^{-4}q_n^{-4} + q_n^{-8}) dq}{\frac{q_{n+1}-q_{n-1}}{2}}$$

$$= \frac{\left(-\frac{q^{-7}}{7} + \frac{2q^{-3}q_n^{-4}}{3} + q_n^{-8}q\right) \big|_{\frac{q_n+q_{n-1}}{2}}^{\frac{q_{n+1}+q_n}{2}}}{\frac{q_{n+1}-q_{n-1}}{2}}$$

$$= \frac{-\frac{1}{7}\left[\left(\frac{q_{n+1}+q_n}{2}\right)^{-7} - \left(\frac{q_n+q_{n-1}}{2}\right)^{-7}\right] + \frac{2q_n^{-4}}{3}\left[\left(\frac{q_{n+1}+q_n}{2}\right)^{-3} - \left(\frac{q_n+q_{n-1}}{2}\right)^{-3}\right] + q_n^{-8}\left(\frac{q_{n+1}-q_{n-1}}{2}\right)}{\frac{q_{n+1}-q_{n-1}}{2}} \qquad \text{Eq-S8}$$

$$\therefore\ g_2\big(q,\Delta t = \infty\big) = 1 + \frac{\langle\big((I(q_n) - \langle I(q_n)\rangle_p\big)^2\rangle_p}{(\langle I(q_n)\rangle_p)^2}$$

$$= 1 + \frac{-\frac{1}{7}\left[\left(\frac{q_{n+1}+q_n}{2}\right)^{-7}-\left(\frac{q_n+q_{n-1}}{2}\right)^{-7}\right]+\frac{2q_n^{-4}}{3}\left[\left(\frac{q_{n+1}+q_n}{2}\right)^{-3}-\left(\frac{q_n+q_{n-1}}{2}\right)^{-3}\right]+q_n^{-8}\left(\frac{q_{n+1}-q_{n-1}}{2}\right)}{\left(\frac{q_{n+1}-q_{n-1}}{2}\right)\left(\frac{1}{q_n^4}\right)^2} \quad \text{Eq-S9}$$
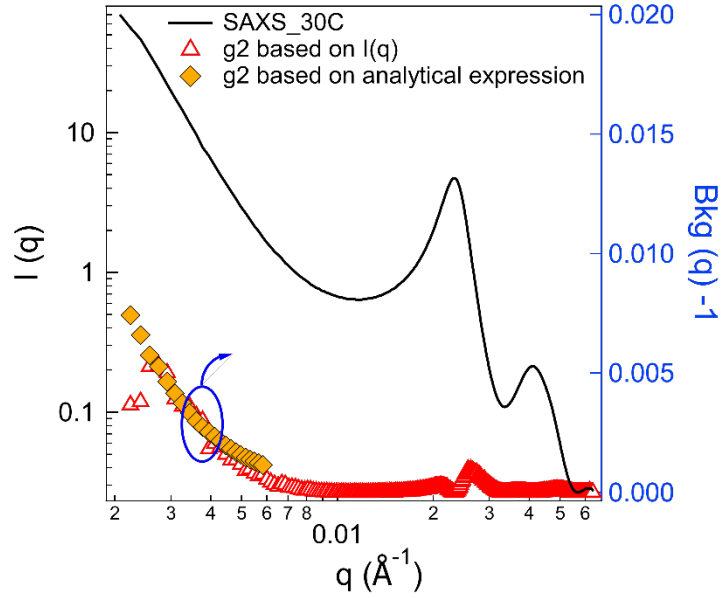

Figure S9. Calculated deviation of Bkg (q)-1 as a function of wavevector q based on SAXS data, as well as on analytical expression I(q) = q^{-4}. The SAXS pattern of SeedGel at 30 ˚C is also plotted.

8. Fitting results from the modeling of XPCS experiments

As discussed in the main text, the intensity correlation functions obtained from the XPCS experiments are fitted with stretched exponential form (Eq-4 in the main text). The non-ergodicity parameter, relaxation time, and stretch exponent are extrapolated from the fitting. Based on the calculations in Figure S9, the background of g_2 is allowed to vary between 1 and 1.005 for q-values smaller than 0.008 Å^{-1}. At q-positions higher than 0.008 Å^{-1}, the background is fixed to 1 for the fittings. Five repeated XPCS measurements are conducted for a sample at each temperature. Each measurement is performed on a fresh spot to avoid beam damage from the X-ray. The fitting results from all five repetitions are summarized in Figures S10 ~ S13 as a function of the wavevector. The results are reproducible and show a consistent trend.
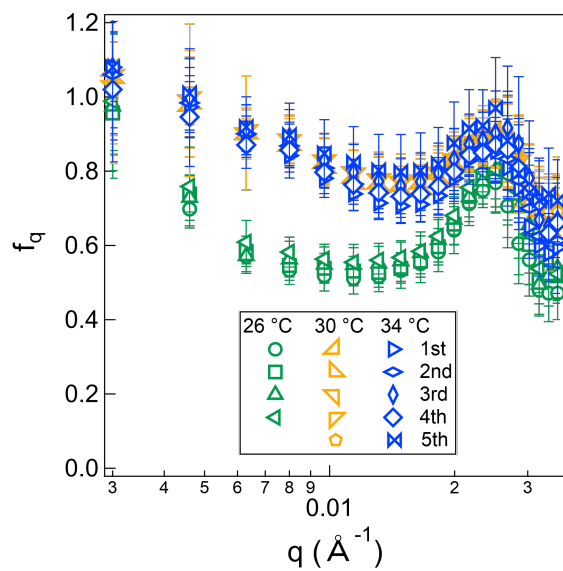
Figure S10. The wavevector dependence of nonergodicity parameter as a function of temperatures at five different spots. The error bars represent one standard deviation.
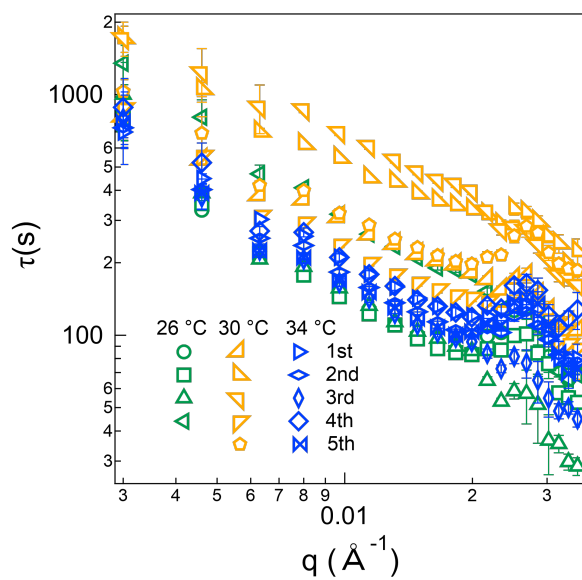

Figure S11. The fitted relaxation time on different locations across the sample at 26 °C, 30 °C, and 34 °C. The error bars represent one standard deviation.

The fitted stretch exponent (β) shown in Figure 4 in the main text is plotted against the wavevector at different temperatures in Figure S12. The results from all the measurements at different positions are summarized in Figure S13. At relatively low temperature (26 ˚C), the SeedGel exhibits stretched exponential relaxation (β < 1). The stretched exponential relaxation transits to compressed exponential relaxation (β > 1) by simply increasing the temperature to 30 ˚C. Such transition is encountered and has been reported in polymer blends and colloidal gels.[15,16] The β value has been used as a measure of the internal stress to explain the temperature-dependent mechanical behavior in polymer nanocomposites. [17]
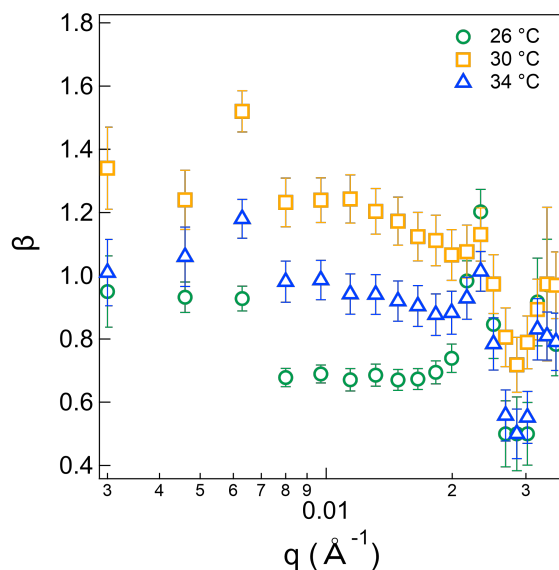

Figure S12. Stretch exponent as a function of wave vector at different temperatures. The error bars represent one standard deviation.
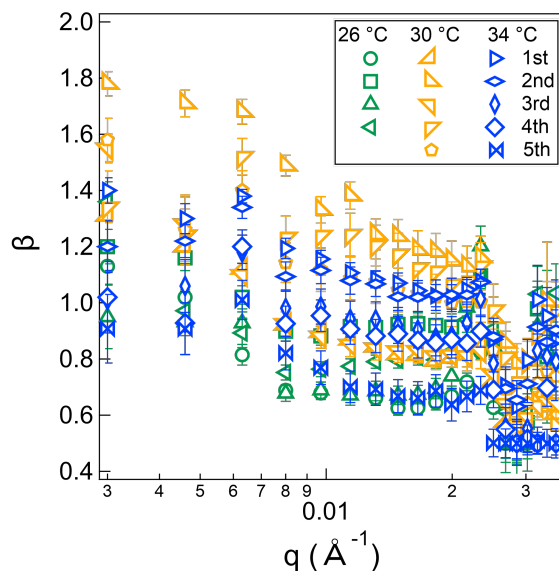
Figure S13. The stretch exponent obtained from fitting XPCS results of SeedGel at five different locations at 26 ˚C, 30 ˚C, and 34 ˚C. The error bars represent one standard deviation.

References:

1 A. Guinier and G. Fournet, *Small-Angle Scattering of X-Rays*, John Wiley and Sons, New York, 1955.
2 J. B. Hayter and J. Penfold, *Molecular Physics*, 1981, **42**, 109–118.
3 J.-P. Hansen and J. B. Hayter, *Molecular Physics*, 1982, **46**, 651–656.
4 M. Kotlarchyk and S. Chen, *The Journal of Chemical Physics*, 1983, **79**, 2461–2469.
5 C. G. Malmberg and A. A. Maryott, *Journal of Research of the National Bureau of Standards*, 1956, **56**, 1.
6 M. Doucet; et al., .
7 Y. Xi, J. B. Leão, Q. Ye, R. S. Lankone, L.-P. Sung and Y. Liu, *Langmuir*, 2021, **37**, 2170–2178.
8 Y. Xi, F. Zhang, Y. Ma, V. M. Prabhu and Y. Liu, *Nat Commun*, 2022, **13**, 3619.
9 H. Guo, G. Stan and Y. Liu, *Soft Matter*, 2018, **14**, 1311–1318.
10 J. R. Villanueva-Valencia, H. Guo, R. Castañeda-Priego and Y. Liu, *Phys. Chem. Chem. Phys.*, 2021, **23**, 4404–4412.
11 Y. Xi, R. S. Lankone, L.-P. Sung and Y. Liu, *Nature Communications*, 2021, **12**, 910.
12 G. Porod, *Kolloid-Zeitschrift*, 1951, **124**, 83–114.
13 L. A. Feigin and D. I. Svergun, *Structure Analysis by Small-Angle X-ray and Neutron Scattering*, Springer, 1987.
14 D. Sheyfer, Q. Zhang, J. Lal, T. Loeffler, E. M. Dufresne, A. R. Sandy, S. Narayanan, S. K. R. S. Sankaranarayanan, R. Szczygiel, P. Maj, L. Soderholm, M. R. Antonio and G. B. Stephenson, *Physical Review Letters*, 2020, **125**, 125504.
15 A. Fluerasu, A. Moussaïd, A. Madsen and A. Schofield, *Physical Review E*, 2007, **76**, 010401.
16 P. Falus, M. A. Borthwick, S. Narayanan, A. R. Sandy and S. G. J. Mochrie, *Physical Review Letters*, 2006, **97**, 066102.
17 R. A. Narayanan, P. Thiyagarajan, S. Lewis, A. Bansal, L. S. Schadler and L. B. Lurio, *Physical Review Letters*, 2006, **97**, 075505.